Electronic Supplementary Information (ESI)

Angled-Stencil Lithography based Metal mesh/$Ti_3C_2T_x$ MXene Hybrid transparent electrodes for Low-power and High-performance Wearable Thermotherapy

Mozakkar Hossain,[a,b] Sibin Kunhi Purayil,[a] K. D. M Rao,*[a,b]

[a.] *School of Applied & Interdisciplinary Sciences, Indian Association for the Cultivation of Science, Jadavpur, Kolkata 700032, India. E-mail: mallik2arjun@gmail.com (K. D. M. R.).*

[b.] *Technical Research Centre, Indian Association for the Cultivation of Science, Jadavpur, Kolkata 700032, India. E-mail: trckdmr@iacs.res.in (K. D. M. R).*

Table of content

1. Schematic illustration and optical microscope images of metal stencil……….Figure S1
2. Large area optical microscope image of Ag micro-mesh…………………….Figure S2
3. Atomic force microscopy analysis of Ag micro-mesh………………………...Figure S3
4. Characterization of Ag and Cu micro-mesh TCEs…………………………....Figure S4
5. Transmission *vs* wavelength of Ag micro-meshes for different thicknesses…Figure S5
6. Transmission *vs* wavelength of Ag meshes at different deposition angles……Figure S6
7. Characterization of $Ti_3C_2T_x$ MXene solution…………………………………Figure S7
8. Details of hybrid Ag micro-mesh/ $Ti_3C_2T_x$ MXene TCE……………………...Figure S8
9. Temperature stability profile with respect to time of hybrid TCE……………Figure S9
10. Details of thickness-dependent angled-stencil lithography……………………Table T1
11. Details of angle-dependent angled-stencil lithography………………………...Table T2
12. Details of Raman vibrational modes of $Ti_3C_2T_x$ MXene thin-film……………..Table T3
13. Details of Thickness dependent sheet resistance and transmittance of MXene..Table T4
14. Details of literature comparison among transparent heaters…………………..Table T5
15. Details of literature comparison among wearable heaters……………….……..Table T6
16. Details of geometrical fill factor calculation of Ag micro-mesh……..……….Section 1
17. Details of the figure of merit calculation of TCEs…….……………………...Section 2
18. Experimental section…………………………………………………………..Section 3

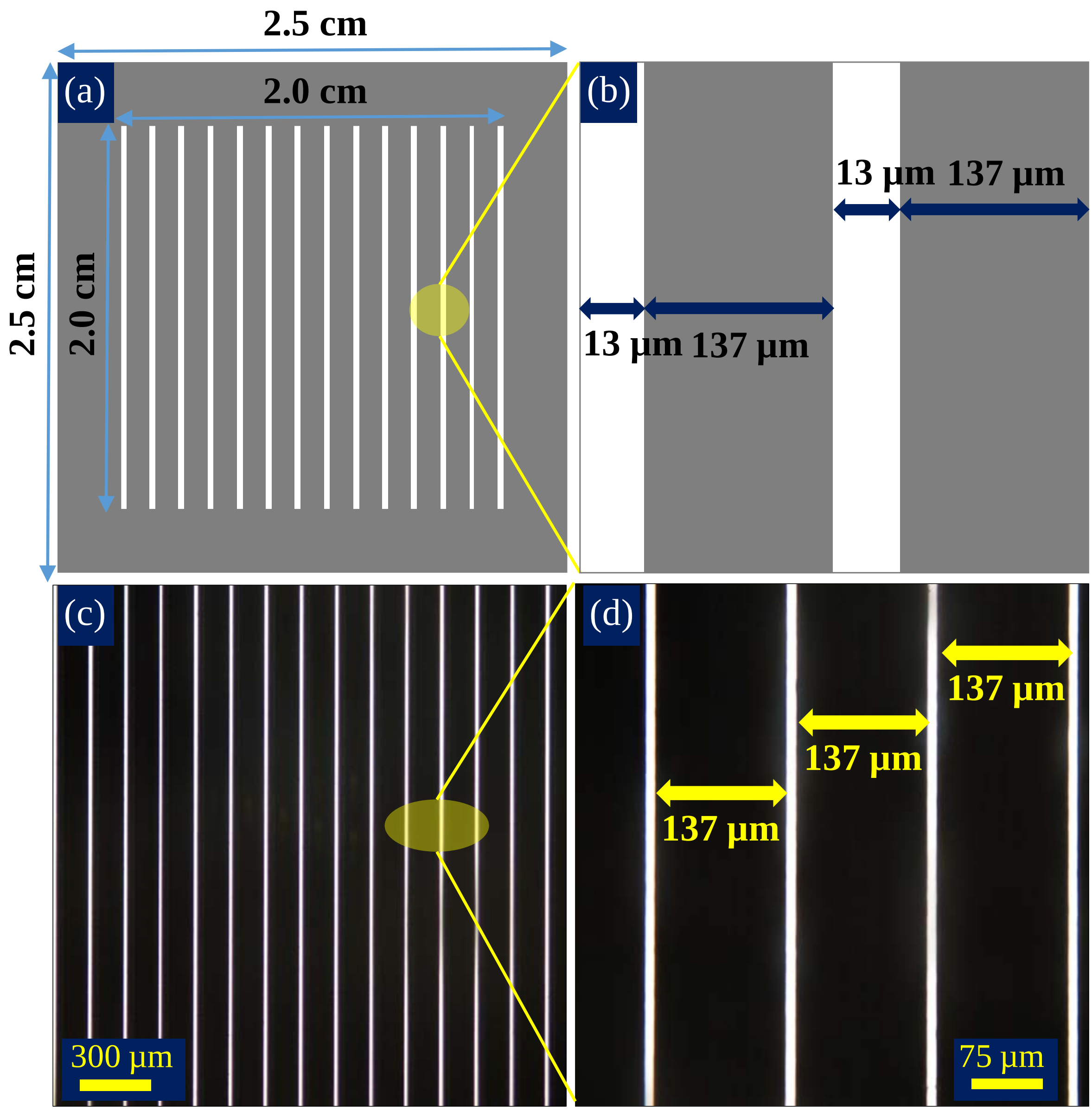

Figure S1. Schematic illustration of the metal stencil, (a) front view, (b) magnified view of two-unit cells. Optical microscope images of metal stencil (c) front view at 5x optical zoom, (d) magnified view.

The metal stencils are essential for angled-stencil lithography to fabricate metal micro-mesh structures. Here, custom-designed metal stencils are adopted as a template. The metal stencil is square with of 2.5 x 2.5 cm^2 area with a thickness of 50 µm where 0.5 cm metal borders are constructed for the stability of the mask (see Figure S1a). The unit cell of the metal stencil consists of a rectangular aperture with 13 µm width, 2 cm length, and a pitch of 137 µm, which are repeated throughout the 2 x 2 cm^2 area. The enlarged schematic in Figure S1b displays two-unit cells of the metal stencil. The large area optical microscope image shown in Figure S1c reveals the repetition of aperture and pitch of the metal stencil. For more clarity, a magnified optical microscopy image is presented in Figure S1d.

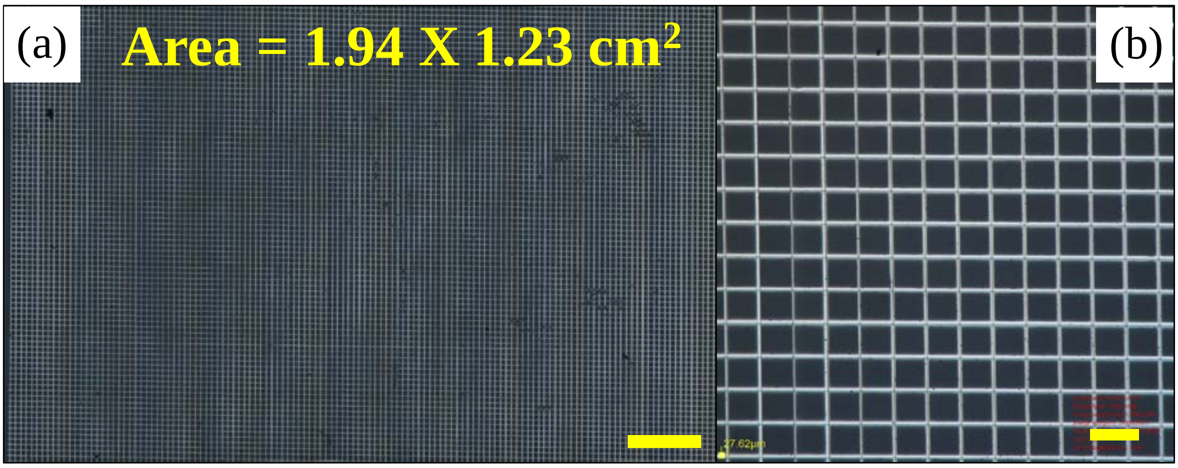

Figure S2. Optical microscope images of Ag micro-mesh, (a) over a large area of 1.94 x 1.23 cm^2, (scale bar 0.2 cm), (b) corresponding magnified image, (scale bar 250 μm).

Optical microscope images of Ag micro-mesh are captured and shown in Figure S2. Figure S2a demonstrates the Ag micro-mesh over a large area of 1.94 x 1.23 cm^2, which confirms the scalability of angled-stencil lithography. The corresponding magnified Optical microscope image is shown in Figure S2b, where the horizontal and vertical microstructures of Ag micro-mesh are highly aligned, resulting in a constant fill factor throughout the mesh structure.

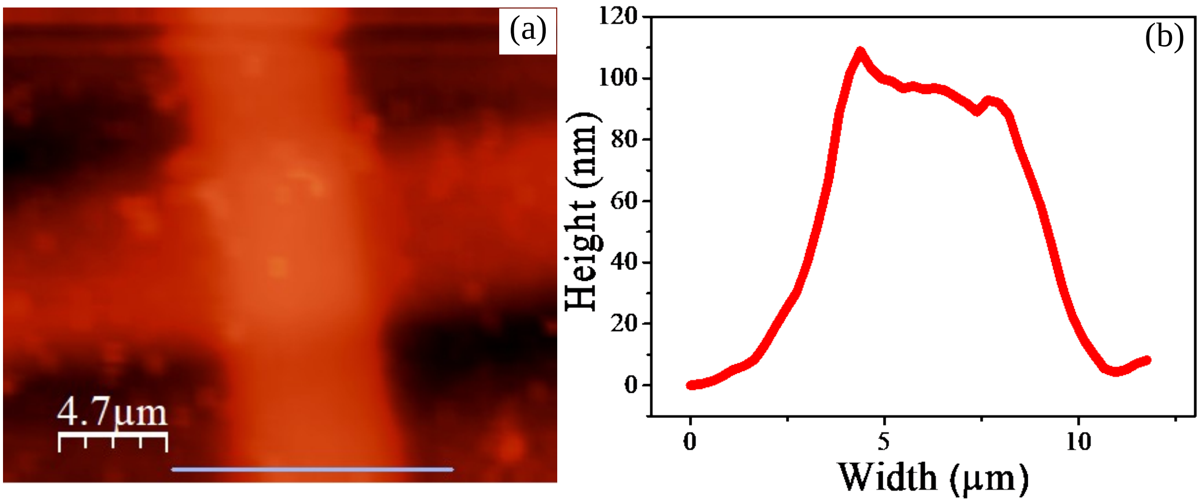

Figure S3. Atomic force microscopy image of (a) a junction in Ag micro-mesh structures, (b) and corresponding height profile.

To evaluate the height of individual microstructures of Ag micro-mesh atomic force microscopy is performed, and corresponding results are presented in Figure S3. AFM image in Figure S3a illustrates a junction of Ag micro-mesh structures consisting of horizontal and vertical microstructures. The height profile extracted from the AFM image is shown in Figure S3b. The individual microstructure thickness is 110 nm.

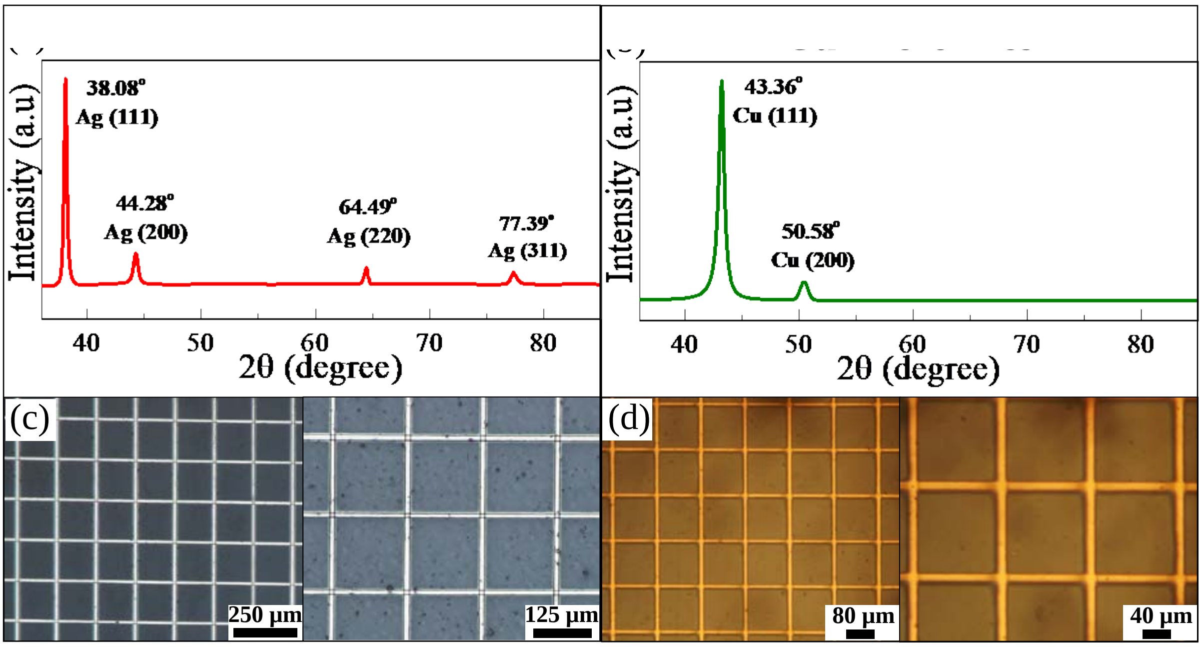

Figure S4. Characterization of metal micro-mesh TCEs (a, b) X-ray diffraction pattern of Ag and Cu micro-mesh based TCEs, respectively, (c, d) corresponding optical microscope images of Ag and Cu micro-mesh TCEs, respectively.

Angled-stencil lithography is a viable solution for fabricating metal micro-mesh TCEs using any refractory metals. As an example, Ag and Cu micro-mesh TCEs are fabricated using angled-stencil lithography (see Figure S4). X-ray diffraction patterns of both the metal micro-meshes are recorded and depicted in Figure S4a and S4b. The diffraction peaks confirm the existence of Ag[1] and Cu[2] metals in the respective micro-meshes. Optical microscope images of Ag and Cu micro-mesh TCEs are captured and shown in Figure S4c and S4d, respectively. It is evident from the images that both the micro-mesh TCEs resemble identical microstructures. Thus, angled-stencil lithography is a universal technique to fabricate metal micro-mesh TCEs without any constraint on source metal.

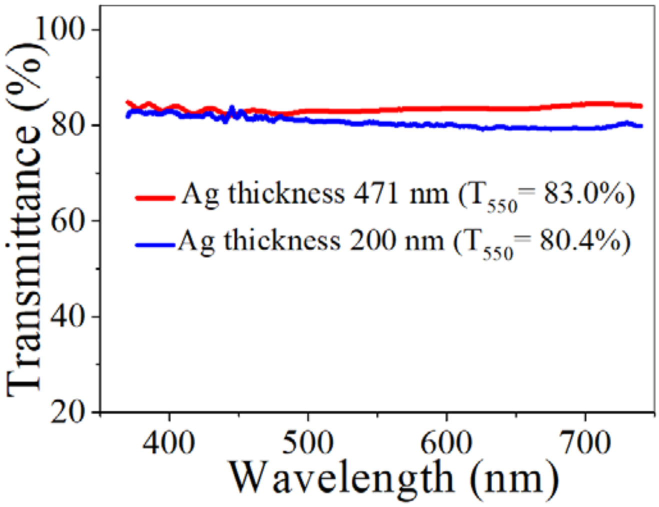

Figure S5. Transmittance as a function of the wavelength of Ag micro-meshes for different thicknesses.

Angled-stencil lithography facilitates the fabrication of the vertical structured metal micro-meshes without any limitation over thickness. Ag micro-mesh of different thicknesses are fabricated, and corresponding transmittance spectra are represented in Figure S5. Despite increasing thickness from 200 to 471 nm, the transmittance of Ag micro-meshes is 80.4 % and 83 % at 550 nm, respectively, which is almost constant. The overall transmittance throughout the visible region also remains constant for both the micro-meshes, respectively. The constant transmittance is attributed to the constant fill factor as a result of angled-stencil lithography.

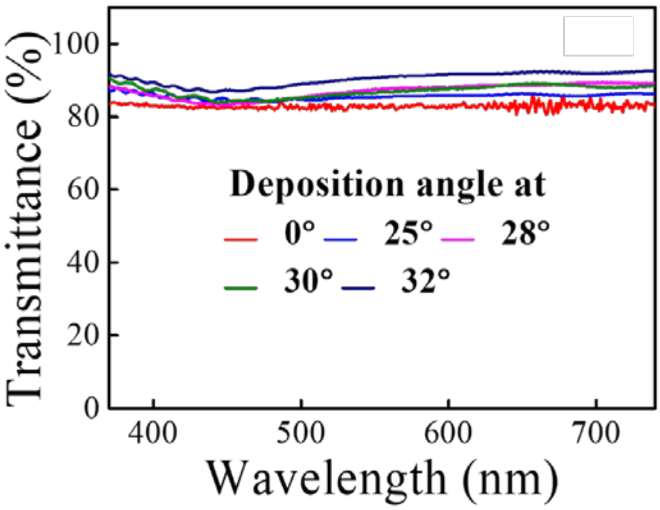

Figure S6. Transmittance as a function of the wavelength of Ag micro-mesh for different deposition angles.

Ag micro-meshes are fabricated at 0°, 25°, 28°, 30°, and 32° deposition angles employing angled-stencil lithography. The transmittance of as-fabricated Ag micro-meshes with different deposition angles are measured in the visible range and presented in Figure S6. The transmittance increases from 83 % to 90 % upon increasing the deposition angle from 0° to 32°, analogous to the decreased fill factor.

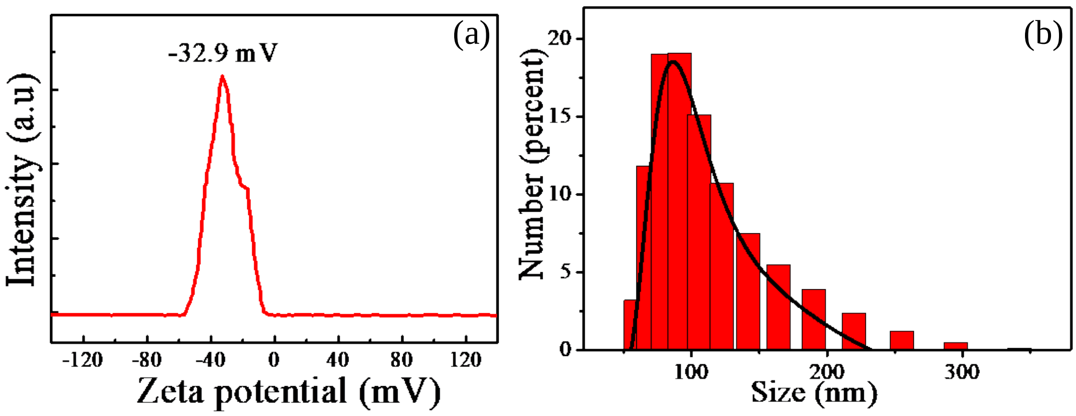

Figure S7. Characterization of $Ti_3C_2T_x$ MXene colloidal solution, (a) zeta potential, (b) particle size distribution.

To characterize the $Ti_3C_2T_x$ MXene colloidal solution, Zeta potential analysis is measured and shown in Figure S7. The zeta potential is found to be -32.9 mV (see Figure S7a), which is close to previously reported zeta potentials of pure $Ti_3C_2T_x$ MXenes.[3] The particle sizes of the $Ti_3C_2T_x$ MXene colloidal solution is analyzed using the dynamic light scattering method and depicted in Figure S7b. The average particle size of the precursor solution is 100 nm, which is suitable for the fabrication of spray-coated $Ti_3C_2T_x$ MXene thin films.

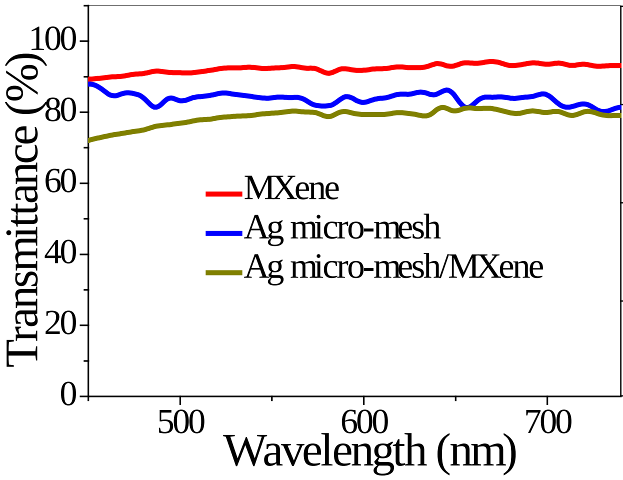

Material	**Sheet Resistance ($\Omega.\square^{-1}$)**	**$T_{550\ nm}$ (%)**
MXene	18.5×10^3	92.4
Ag-micro mesh	0.8	84.0
Ag-micro mesh/MXene	1	79.7

Figure S8. Transmission as a function of wavelength for hybrid Ag micro-mesh/$Ti_3C_2T_x$ MXene TCE and $Ti_3C_2T_x$ MXene, Ag micro-mesh. Corresponding sheet resistances are tabulated.

Hybrid Ag micro-mesh/ $Ti_3C_2T_x$ MXene TCEs are fabricated using angled-stencil lithography followed by spray coating of $Ti_3C_2T_x$ MXene. The transmittance and sheet resistance of pristine Ag micro-mesh TCE and hybrid TCE are measured, as shown in Figure S8. Spray coated pristine $Ti_3C_2T_x$ MXene thin films exhibit a transmission of 92.7 % at 550 nm with a sheet resistance of $18.3 \times 10^3\ \Omega.\square^{-1}$. The transmittance and sheet resistance of hybrid TCE is 79.7 % and $1\ \Omega.\square^{-1}$, respectively. The reduction in transmittance is attributed to the absorption of the $Ti_3C_2T_x$ MXene thin film layer.

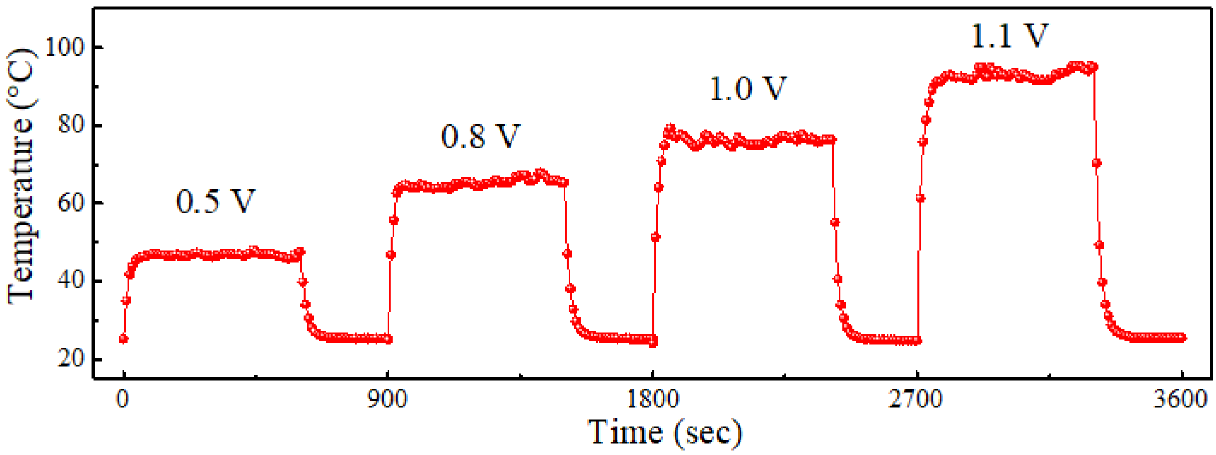

Figure S9. Temperature stability profile with respect to time at different applied biases 0.5, 0.8, 1.0, and 1.1 V of the hybrid Ag micro-mesh/$Ti_3C_2T_x$ MXene transparent heaters.

The hybrid heaters are applied with modulated bias from 0.5 V to 1.1 V and examined the temperature stability with respect to time as depicted in Figure S9. The hybrid transparent heater reached steady state temperature of 46.4, 66.1, 75.3 to 94.9 °C with the applied bias of 0.5, 0.8, 1.0 to 1.1 V, respectively. In each cycle, the acquired temperatures are steady throughout 600 s until the bias is turned off. The temperature profile of hybrid heater is examined for prolong duration of 3.6×10^3 s. Thus, the hybrid Ag micro-mesh/$Ti_3C_2T_x$ MXene based transparent heaters demonstrated remarkable heating stability.

Table T1: Details Ag micro-mesh TCEs with different thicknesses.

SL No	Material	Deposition Angle (°)	Thickness (nm)	T_{550nm} (%)	Sheet -resistance (Ω/□)	FOM
1	Ag	0	110	82.9	2.3	785
2	Ag	0	200	80.4	2	798
3	Ag	0	471	83	0.8	2.4×10^3

Table T2. Variation of wire width and geometrical fill factor of Ag micro-mesh as a function of deposition angle.

Deposition Angle (°)	Wire Width (μm)	Geometrical Fill Factor (%)
0	13	16.5
25	8.91	11.52
28	7.6	9.87
30	6.1	7.96
32	4.4	5.78

Table T3. Details of Raman vibrational modes of $Ti_3C_2T_x$ MXene thin-film.

Raman shift (cm^{-1})	$Ti_3C_2T_x$ MXene	Vibration mode
201	$Ti_3C_2O_2$	ω1 (A_{1g})
375	$Ti_3C_2O_2$	ω4 (E_g)
514	$Ti_3C_2(OH)_2$	ω6 (A_{1g})
592	$Ti_3C_2O_2$	ω5 (A_{1g})
627	$Ti_3C_2(OH)_2$	ω4 (E_g)
693	$Ti_3C_2F_2$	ω3 (A_{1g})

The functional groups in $Ti_3C_2T_x$ MXene are one of the fundamental elements to enrich the performance of $Ti_3C_2T_x$ MXene. The formation of pure $Ti_3C_2T_x$ MXene in the phase is confirmed by XRD analysis. in the thin film, Raman spectra of $Ti_3C_2T_x$ MXene thin film is captured to examine surface functional groups (see Table T1).[4-5]

Table T4: Comparation of thickness dependent sheet resistance and transmittance for the pristine $Ti_3C_2T_x$ MXene and hydride TCE.

S.No.	Material and thickness	Transmittance at 550 nm	Sheet resistance (kΩ/□)
1.	$Ti_3C_2T_x$ MXene with 15 nm	95%	100
2.	$Ti_3C_2T_x$ MXene with 25 nm	92%	18
3.	$Ti_3C_2T_x$ MXene with 60 nm	53%	0.5
4.	Ag micro-mesh	83%	0.8
5.	Ag micro-mesh with 25 nm $Ti_3C_2T_x$ MXene	79.8%	1

Table T5. Literature comparison of transparent heaters and their performance.

SL No	Active Material	Process	*T_{550nm} (%)	Voltage (V)	Power (W/cm^2)	Peak Temp (°C)	SR (Ω/□)	FOM	Thermal resistance (°C $cm^2.W^{-1}$)	Ref No
1	AgNW-PEDOT:PSS /ITO	Slot-die-coated	95	11	0.4	115	41	176	210	6
2	Au mesh	Photo-Lithography	80	> 5.5	0.5	150	5	336	249	7
3	Ag mesh	Crackle Lithography	77	8.5	0.57	170	1	1350	255	8
4	Pt mesh	Photo-lithography Lift-off	89	5	0.18	69	94	33.4	258	9
5	Ag mesh	Crackle Network	86	<5	0.13	100	6	401	515	10
6	Ag CP	Crackle Network	86	---	0.20	110	7	343	420	11
7	AgNW PEDOT:PSS	Solution Process	70	6	0.25	110	4	241	179	12
8	AgNW/PU	Spin/Spray Coating	77	6	0.75	102	13	103	100	13
9	PEDOT:Sulf	Spin Coating	87.8	12	0.24	138	57	50	384	14
10	Ag Nano Fibers	Electrospinning	83	4.5	0.65	250	0.5	3861	346	15
11	Au Mesh	Crackle-template	87	15	2.8	600	5.4	472	189	16
12	Ag Nanotrough	Thermal evaporation/ Electrospinning	87	7	0.30	100	23	114	276	17
13	Pd Network	Crackle lithography	80	9	0.85	75	200	7.98	100	18
14	SWNTs	Solution Process	90	7	0.26	100	93	37.4	187	19
15	Polymer mesh	Photopatterning	85	3	0.18	69	10	220	255.9	20
16	Ag micro-mesh	Angled-Stencil Lithography	82	2.3	0.12	99	5.38	335.8	506.6	This Work
17	Ag micro-mesh/$Ti_3C_2T_x$ MXene	Angled-Stencil Lithography	80	1.2	0.10	99	1.6	998	675	This Work

*T_{550nm} = transmittance at 550 nm

The Ag micro-mesh/$Ti_3C_2T_x$ MXene transparent heater fabricated through angled-stencil lithography demonstrated low power consumption of 0.10 W/cm^2 resulting in record-high thermal resistance of 675 °C cm^2.W^{-1}, low actuation voltage of 1.2 V, and ultra-low power consumption among transparent heaters fabricated in literature including Ag NW-PEDOT:PSS[6,12], Metal meshs[7-11,16,18], Ag NW/PU[13], PEDOT:Sulf[14], AgNano Fibers[15], Ag Nanotrough[17], SWNTs[19], Polymer mesh[20].

Table T6. Literature comparison of Wearable heaters performance.

SL No	Active Material	Process	Transparent/ Opaque	*T_{550nm} (%)	Voltage (V)	Power (W/cm^2)	Peak Temp (°C)	SR (Ω/□)	Ref No
1	ANF/Ag NW nanocomposite	vacuum assisted filtration/ hot-pressing	Transparent	40	1.5	0.41	200	0.40	1
2	Ag Nano Fibers	Electrospinning	Transparent	83	4.5	0.65	250	0.5	15
3	CuZr MG Nano trough	Electrospinning/ Co-sputtering	Transparent	90	7	3.2	180	3.8	21
4	Ag NW Film	Supersonic cold spraying	Transparent	95	6	0.27	180	15	22
5	Al Paper	Spin coating	Opaque	---	1.5	5.95	50	0.075	23
6	Weft-knitted carbon fabric	Heat Treatment process	Opaque	----	3	0.30	150	1.89	24
7	LM@PDMS	direct ink writing	Opaque	---	3.5	0.15	100	8.88	25
8	MXene-decorated polymeric textile	Dip Coating	Opaque	---	2.5	0.31	200	5	26
9	Ag micro-mesh/$Ti_3C_2T_x$ MXene	Angled-Stencil Lithography	Transparent	80	1.3	0.12	99	1.7	This Work

*T_{550nm} = transmittance at 550 nm

Section 1. Geometrical Fill factor calculation of Ag micro-mesh.

The fill factor of Ag micro-meshes is estimated using the following equation.[27]

$$FF = \frac{(p \times w)+[(p-w) \times w]}{p^2} \text{----------------------(1)}$$

Where FF = geometrical fill factor (percentage of material present in the micro-mesh),

w = line width of the individual microstructure of Ag micro-mesh,

p (pitch size) = distance between two consecutive microstructures,

The geometrical fill factor is a mathematical calculation to predict the percentage of material. Here, the percentage of metallic conduits present in Ag micro-mesh TCEs are estimated using FF.

Section 2. Figure of merit calculation of TCEs.

The figure of merit of a transparent conducting electrode can be evaluated from the following equation.[28]

$$FOM = \frac{188.5}{R_S * (\frac{1}{\sqrt{T}} - 1)} \text{------------------------------ (2)}$$

Where, FOM (Figure of Merit) = $\frac{\sigma_{dc}}{\sigma_{opt}}$ = ratio of electrical conductance to optical conductance,

R_S = sheet resistance of the TCE,

T = transmittance of the TCE at 550 nm.

The figure of merit (FOM) is a tool to evaluate the performance of TCEs. It is defined as the ratio of electrical conductance to optical conductance. To meet the requirement of TCEs, the minimum value of FOM is 35, and the average TCE FOM values are around 350.

Section 3. Experimental Section.

3.1. Materials:

Ti_3AlC_2 is purchased from Y-carbon. Ag, Cu, LiF, and HCl were purchased from Sigma-Aldrich. Silicone oil is purchased from Loba chemicals. The metal stencils are designed as mentioned earlier, and purchased from Harshini Industries from Bangalore. All the chemicals were used without further purification.

3.2. Fabrication of metal-micro mesh TCEs:

The Glass/PET substrates are cleaned in soap water and ultrasonicated in Milli-Q water, acetone, and isopropanol for 10 minutes each, respectively. The Glass/PET substrates of 2.5 x 2.5 cm^2 were conformally attached with metal stencils and placed inside the physical vapor deposition system (Hind High Vacuum Company Private Limited: model:12A4D). The metals are placed in a molybdenum boat inside a vacuum chamber, which is maintained at ~ (1-3) $\times 10^{-6}$ m. bar pressure. The Ag and Cu metals were evaporated, respectively, by maintaining the deposition rate between 5-10 Å/s. After performing the first metal deposition, the stencil is rotated 90° and reattached with the substrate and reinsertion in the vacuum chamber to execute the 2^{nd} metal deposition. To decrease the width of microstructures during the angled-stencil lithography, the deposition angle between sublimated metal flux and metal stencil containing substrate is varied from 0° to 32° using a custom-designed substrate holder.

3.3 Synthesis of $Ti_3C_2T_x$ MXene nanosheets:

9M 10 ml HCL solution is kept in the silicone bath to acquire 35°C using a hotplate (Tarsons). 0.8 g LiF powder is mixed in HCl solution using a magnetic stirrer at 600 RPM for 10 minutes. Then 0.5 g Ti_3AlC_2 powder is slowly added to the mixture, which is maintained at 35°C and 600 RPM for 24 hours. The acidic suspension is diluted with Milli-Q water to make a total 40 ml solution. The diluted acidic suspension is centrifuged multiple times at 3500 RPM for 5 minutes until pH ~ 6 is achieved. After each centrifugation cycle, the supernatant solution is replaced with fresh Milli-Q water. After reaching pH = 6, the dark green $Ti_3C_2T_x$ MXene nanosheet suspension is collected for spray coating. The $Ti_3C_2T_x$ MXene colloidal dispersion is prepared by mixing (50-70 µl) $Ti_3C_2T_x$ MXene supernatant (930-950 µl) in Milli-Q water.

3.4 Fabrication of hybrid Ag-micro mesh/ $Ti_3C_2T_x$ MXene TCEs:

Hybrid Ag-micro mesh/$Ti_3C_2T_x$ MXene TCEs are fabricated using angled-stencil lithography followed by spray coating of $Ti_3C_2T_x$ MXene dispersion. During spray coating, 20 psi N_2 pressure is maintained, and the Ag micro-mesh substrate is kept at an elevated temperature of 50 °C. The $Ti_3C_2T_x$ MXene dispersion is spray-coated for 0.5 s and dried for 3-4 s using a hot air gun. The same processor is repeated until the $Ti_3C_2T_x$ MXene thin film is formed.

3.5 Fabrication of transparent heater and portable thermotherapy device:

Transparent heaters and thermotherapy devices are prepared with hybrid Ag-micro mesh/ $Ti_3C_2T_x$ MXene TCEs. The total area of the devices is 2.5 x 2.5 cm^2. Two copper wires are connected at the two opposite sides of the hybrid TCEs using silver paste. For the fabrication of a portable thermotherapy device, the as-prepared transparent heater on PET substrate is mounted on a transparent and thermally conducting 3M tape and affixed to the wrist. The compact and portable power supply is assembled by connecting a 3.7 V lithium polymer battery (KP 301523 250 mAh), switch (NC KCD-002), and a variable potentiometer (Alps Alpine, 729-3420, RK09L1140A65) in a 5.5 x 3.5 cm^2 box. The variable potentiometer is used to control the power to generate the required heating temperature for healing.

3.6 Characterization of Metal micro-mesh, $Ti_3C_2T_x$ MXene, hybrid transparent heater, thermotherapy device:

XRD diffraction pattern of samples is performed in PAN analytical (X'Pert PRO, 40 kV, 30 mA, wavelength ~ 0.154 nm) and Bruker AXS D8 Advanced equipment (40 kV, 40 mA, wavelength ~ 0.15406 nm) with Cu Kα radiation. Optical microscope images are captured using Olympus microscopes (BX-51 and DSX 510). The alignment of the mesh structures is analyzed using FFT in Gwydion 64-bit software. $Ti_3C_2T_x$ MXene is characterized by depositing thin films on the glass/PET substrate. Raman spectroscopy of $Ti_3C_2T_x$ MXene is performed using Raman Triple spectrometer Jobin-Yvon T64000 by exciting the sample with Nd: YAG green laser (532.5 nm, ~ 1 mW power). The thickness of the samples is measured using Vecco, di CP-II and Asylum Research MFP-3D AFM in tapping mode. Zeta potential and particle size distribution of $Ti_3C_2T_x$ MXene are analyzed using the Dynamic Light Scattering method at a pH of 7 (ZEN3600). The transmission measurements of the samples are performed in UV-VIS-Agilent 8453 UV-visible Spectroscopy System with reference to the glass/PET substrate. The sheet resistance of metal micro-meshes, $Ti_3C_2T_x$ MXene, and hybrid TCEs is estimated with Keithley 2634B SMU in two probe configurations. Comparison of the charging effect between pristine Ag micro-mesh and hybrid Ag micro-mesh/MXene is visualized with FESEM (JEOL JSM-7500F). A blue LED is used to demonstrate the electrical and mechanical performance of the hybrid TCE. The transparent heaters are powered with a DC voltage source (HTC instruments DC 3002-II), and temperatures are recorded using a k-type thermocouple (Thermometer: Version 1312-EN-00, FLIR ONE PRO, and FLIR E5 thermal imaging cameras. The thermal images/video of the transparent heaters and the thermotherapy devices are captured using FLIR ONE PRO, a thermal imaging camera.

Notes and references

1 Z. Ma, S. Kang, J. Ma, L. Shao, A. Wei, C. Liang, J. Gu, B. Yang, D. Dong, L. Wei, and Z. Ji, *ACS Nano*, 2019, **13**, 7578−7590.

2 L. Zhao, S. Yu, X. Li, M. Wu, and L. Li, *Org. Electron.*, 2020, **82**, 105511.

3 H. Tang, H. Feng, H. Wang, X. Wan, J. Liang, and Y. Chen, *ACS Appl. Mater. Interfaces*, 2019, **11**, 25330–25337.

4 T. Hu, J. Wang, H. Zhang, Z. Li, M. Hu and X. Wang, *Phys. Chem. Chem. Phys.*, 2015, **17**, 9997–10003.

5 Z. Wang, H. Kim, and H. N. Alshareef, *Adv. Mater.*, 2018, **30**, 1706656.

6 J. Park, D. Han, S. Choi, Y. Kim and J. Kwak, *RSC Adv.* 2019, **9**, 5731–5737.

7 E. Thouti, C. Mistry, A. Chandran, D. Kumar Panwar, P. Kumar, H. Suman and J.

Akhtar, *J. Phys. D. Appl. Phys.* 2019, **52**, 425301.

8 S. Kiruthika, R. Gupta and G. U. Kulkarni, *RSC Adv.* 2014, **4**, 49745–49751.

9 D. Lordan, M. Burke, M. Manning, A. Martin, A. Amann, D. O'Connell, R. Murphy, C. Lyons and A. J. Quinn, *ACS Appl. Mater. Interfaces*, 2017, **9**, 4932–4940.

10 R. Gupta, K. D. M. Rao, K. Srivastava, A. Kumar, S. Kiruthika and G. U. Kulkarni, *ACS Appl. Mater. Interfaces*, 2014, **6**, 13688–13696.

11 K. D. M. Rao, R. Gupta and G. U. Kulkarni, *Adv. Mater. Interfaces*, 2014, **1**, 1400090.

12 S. Ji, W. He, K. Wang, Y. Ran and C. Ye, *Small*, 2014, **10**, 4951–4960.

13 N. Tiwari, Ankit, M. Rajput, M. R. Kulkarni, R. A. John and N. Mathews, *Nanoscale*, 2017, **9**, 14990–14997.

14 M. N. Gueye, A. Carella, R. Demadrille and J. P. Simonato, *ACS Appl. Mater. Interfaces*, 2017, **9**, 27250–27256.

15 J. Jang, B. G. Hyun, S. Ji, E. Cho, B. W. An, W. H. Cheong and J.-U. Park, *NPG Asia Mater.* 2017, **9**, e432.

16 K. D. M. Rao and G. U. Kulkarni, *Nanoscale*, 2014, **6**, 5645–5651.

17 P. Li, J. G. Ma, H. Y. Xu, D. Lin, X. D. Xue, X. Z. Yan, P. Xia and Y. C. Liu, *J. Alloys Compd.*, 2016, **664**, 764–769.

18 S. Walia, R. Gupta, K. D. M. Rao and G. U. Kulkarni, *ACS Appl. Mater. Interfaces*, 2016, **8**, 23419–23424.

19 Y. Kim, H. R. Lee, T. Saito and Y. Nishi, *Appl. Phys. Lett.* 2017, **110**, 153301.

20 N. S. Jang, S. H. Jung, E. J. An, J. W. Oh, H. M. Lee and J. M. Kim, *J. Mater. Chem. C*, 2019, **7**, 9698–9708.

21 B. W. An, E. J. Gwak, K. Kim, Y. C. Kim, J. Jang, J. Y. Kim and J. U. Park, *Nano Lett.*, 2016, **16**, 471–478.

22 J. G. Lee, J. H. Lee, S. An, D. Y. Kim, T. G. Kim, S. S. Al-Deyab, A. L. Yarin and S. S. Yoon, *J. Mater. Chem. A*, 2017, **5**, 6677–6685.

23 N. S. Jang, K. H. Kim, S. H. Ha, S. H. Jung, H. M. Lee and J. M. Kim, *ACS Appl. Mater. Interfaces*, 2017, **9**, 19612–19621.

24 M. Zhang, C. Wang, X. Liang, Z. Yin, K. Xia, H. Wang, M. Jian and Y. Zhang, *Adv. Electron. Mater.*, 2017, **3**, 1700193.

25 Y. Wang, Z. Yu, G. Mao, Y. Liu, G. Liu, J. Shang, S. Qu, Q. Chen and R. W. Li, *Adv. Mater. Technol.*, 2019, **4**, 1800435.

26 X. Liu, X. Jin, L. Li, J. Wang, Y. Yang, Y. Cao and W. Wang, *J. Mater. Chem. A*, 2020, **8**, 12526–12537.

27 H. B. Lee, W. Y. Jin, M. M. Ovhal, N. Kumar, and J. W. Kang, *J. Mater. Chem. C*, 2019, **7**, 1087–1110.

28 H. J. Kim, S. H. Lee, J. Lee, E. S. Lee, J. H. Choi, J. H. Jung, J. Y. Jung and D. G. Choi, *Small*, 2014, **10**, 3767–3774.